Compact Lithium Niobate Electrooptic Modulators

Ashutosh Rao, *Student Member, IEEE*, and Sasan Fathpour, *Senior Member, IEEE*

(Invited Paper)

***Abstract*—Lithium niobate (LN), spurred by its success for fiber-optic communications, has remained the material of choice for high-performance electrooptic (EO) modulators. The past decade has seen a surge in efforts aimed at miniaturizing LN EO modulators with higher order modulation formats, data centers, and optical interconnect applications in mind. The state-of-the-art of these compact modulators, with a focus on fabrication, design, and high-speed performance is reviewed. Guidelines for design optimization and key performance metrics of these important integrated photonic devices are presented. Furthermore, an outlook on the road toward commercial viability, along with potential novel applications is provided.**

***Index Terms*—Electrooptic modulation, optical waveguides, microwave photonics, nanophotonics, optical fiber communication, photonic integrated circuits, silicon photonics, electrooptic devices.**

I. Introduction

LITHIUM niobate (LN) electrooptic (EO) modulators are widely available as packaged commercial off-the-shelf (COTS) components from several suppliers (e.g., [1]–[6]). Numerous technological advances followed the development of LN EO modulators for high-speed communications [7]–[9] and optical switches [10]–[12]. Waveguide propagation loss [13], [14], coupling loss [15]–[17] and thermal and direct current (DC) drift effects [18]–[20] have been suppressed along with advances in packaging. Modulation bandwidths are increased thanks to improved radio-frequency (RF) design considerations [21]–[25]. Finally, the development of erbium-doped fiber amplifiers was instrumental in the deployment of long-haul optical transmission systems, in which LN EO modulators play a central role and have enjoyed tremendous success [26]–[28].

Meanwhile, coherent optical transmission has been advanced by wavelength division multiplexing (WDM) [29]–[31] and higher order modulation formats [32], [33]. More recently, short reach optical interconnects have become important for data centers [34]–[36], and for potential integration with electronics [37], [38]. The ability to form compact optical modulators, and integrate many of them on a chip is vital to the continued development of these domains.

The low-loss stripe waveguides of COTS LN EO modulators are usually formed by proton exchange (PE) [39]–[41] or in-diffusion of titanium [13]–[15], [42]. These low-index-contrast waveguides present poor optical confinement leading to certain diminished performances, particularly high drive voltages, length and bending radii [43]. These factors render them incompatible with the fundamental philosophies of modern integrated photonics – compact devices, low drive voltages and power consumption, small bending radii, and dense on-chip integration. Nonetheless, they present remarkable modulation bandwidths, in excess of 100 GHz, and excellent performance, e.g., high extinction ratio for digital and high linearity for analog applications [42], [44]. These positive attributes have motivated the pursuit of solutions for the aforementioned shortcomings, towards the realization of miniaturized LN EO modulators–the focus of this review paper.

For completeness, we mention that LN is not the only material pursued for compact modulator applications. The free-carrier plasma-dispersion effect (sometimes wrongly confused with the true EO or Pockel's effect) has been used in silicon-on-insulator (SOI) waveguides to form modulators [45]–[47]. Electroabsorption (EA) modulators on III-V compound semiconductors, e.g., indium phosphide (InP) [48]–[50] as well as silicon-germanium (SiGe) [51], [52], are well-established, and have been heterogeneously integrated on the SOI platform [51]–[53]. Spin-on EO polymers have been used on the SOI platform as well [54]–[56]. Each of these approaches has its benefits and shortcomings. Silicon optical modulators can be directly formed on SOI wafers using CMOS-compatible processing, but at the cost of limited dynamic electrical extinction [57], [58] and linearity [59]. III-V EA modulators also usually present low extinction ratios [60] and generally have larger cross-sections than the silicon plasma dispersion modulators, leading to much larger bending radii. The reliability of polymer EO modulators has been a concern, although stable high temperature operation has recently been demonstrated [61]. A detailed comparison on the technical pros and cons of all these different platforms and predictions on their commercial success and potential market share is beyond the scope of this work; this paper focuses on compact LN modulators.

Section II describes the fabrication of compact LN EO modulators. Section III reviews the state of the art and touches upon digital and analog system requirements. Section IV addresses

Manuscript received October 9, 2017; revised November 28, 2017; accepted November 29, 2017. Date of publication December 4, 2017; date of current version January 8, 2018. This work was supported in part by the U.S. Office of Naval Research Young Investigator Program, in part by the Department of Energy, in part by the National Science Foundation, and in part by Harris Corporation. *(Corresponding author: Sasan Fathpour.)*

A. Rao is with the Center for Research and Education in Optics and Lasers, The College of Optics and Photonics, University of Central Florida, Orlando, FL 32816 USA (e-mail: ashutoshrao@knights.ucf.edu).

S. Fathpour is with the Center for Research and Education in Optics and Lasers, The College of Optics and Photonics, and also with the Department of Electrical and Computer Engineering, University of Central Florida, Orlando, FL 32816 USA (e-mail: fathpour@creol.ucf.edu).

Color versions of one or more of the figures in this paper are available online at http://ieeexplore.ieee.org.

Digital Object Identifier 10.1109/JSTQE.2017.2779869

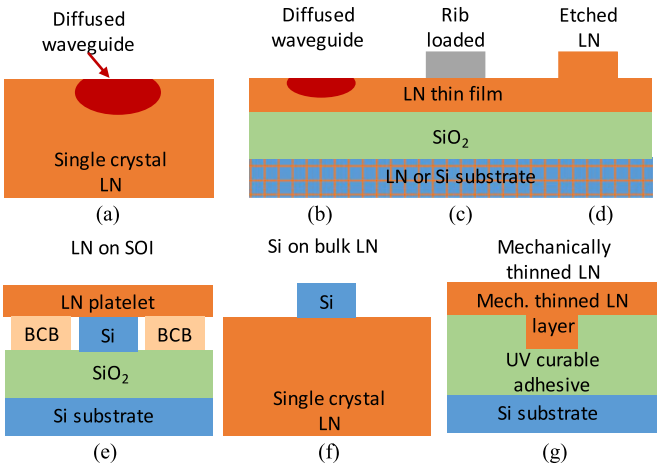

Fig. 1. (a) Conventional diffused LN waveguide with low confinement and large mode area; (b)-(d) LN-on-SiO_2 waveguides (on either LN or Si substrates): (b) proton exchanged, (c) rib loaded, and (d) dry etched; (e) LN platelets bonded on top of SOI waveguides; (f) Silicon-on-LN waveguides; (g) Mechanically-thinned LN waveguides adhesive-bonded to silicon.

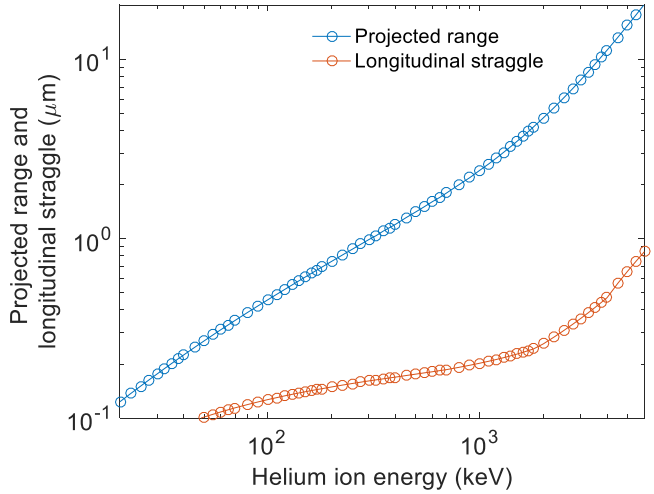

Fig. 2. Variation of projected range and longitudinal straggle with helium ion implantation energy.

the design of such modulators. Section V outlines advances required for commercial viability and potential applications, and Section VI presents our concluding remarks.

II. Waveguide Platforms and Their Fabrication

Cross-sectional schematics of the major modern LN waveguide platforms developed in recent years and used for modulators are shown in Fig. 1. A schematic of conventional diffused waveguides in bulk LN single crystals (Fig. 1(a)) is also shown.

Fig. 1(b)–(d) depict three approaches for forming thin-film waveguides on thermally-exfoliated thin-film LN on SiO_2. They are proton-exchange, rib-loading with a different material, and dry etching of LN, respectively. These thin-film LN wafers are commercially available in 75-mm diameter on both LN and Si substrates. We expect that these thin film LN wafers will likely be available in 150 mm diameter in the near future – single-crystalline LN wafers are commercially available up to 150 mm, and the bonding technology is sufficiently mature.

A different approach, enabled by the maturation of thermally exfoliated LN thin film technology, is shown in Fig. 1(e). Here, sub-micrometer-thick platelets of LN are bonded on SOI using special transfer techniques, which do not damage the thin platelets. The Si on LN platform, shown in Fig. 1(f), employs a different approach of patterning thin films of silicon on bulk LN substrates. Both single-crystalline and amorphous thin films have been utilized, as discussed later. Finally, Fig. 1(g) shows an approach based on mechanical thinning or polishing. A patterned LN wafer is adhesive-bonded to a Si wafer. The LN substrate is mechanically thinned down to form the thin film. In the following, the fabrication of compact modulators on these platforms is discussed.

A. Substrate Fabrication

The first step towards realizing compact EO modulators and other devices using LN is the ability to slice thin films of single crystal LN from bulk LN wafers and bond them to transparent low refractive index substrates, while maintaining the EO property of LN. This approach has provided superior ferroelectric thin film quality compared to other approaches, such as molecular beam epitaxy [62], pulsed laser deposition [63], sputtering [64], chemical vapor deposition [65], and sol-gels [66]. Since LN is anisotropic, the crystal orientation of a wafer is of paramount importance to realize the desired EO effect. LN wafers are commercially available with many different orientations. Among them, *X*, *Y* and *Z*-cut wafers are important for photonic applications.

The workhorse of forming thin films of LN, exploited in the approaches of Fig. 1(b)–(e), is helium (He) ion implantation. A crystalline LN surface is bombarded with He ions at a specific angle, energy, and dose. The ions lose their energy to the LN crystal, through nuclear collisions and electronic excitation, and stop at a particular penetration depth, where they damage and thereby physically weaken the crystal. This depth is characterized by a variety of statistical measures. Its average and deviation are called the projected range and longitudinal straggle, respectively. The dependence on He ion energy is shown in Fig. 2, estimated using a Monte-Carlo simulation package [67]. The projected range provides an initial estimate of the final thin-film thickness, while the longitudinal straggle is indicative of the size of the implanted or damaged layer. There are two methods to forming thin films of LN using He-ion implantation, as follows.

1) Crystal Ion Slicing: The first method based on ion implantation, called crystal ion slicing (CIS), was established in the late 1990s. A single crystal LN wafer is implanted with He ions at a few MeV, annealed, and wet-etched in hydrofluoric acid, to detach a single crystal free-standing LN thin film. Rapid thermal annealing is used to recover the material properties of LN which are degraded after the implantation step [68]. CIS is suited for LN films around 10-μm thick. The spatially non-uniform exposure to the wet etchant across a die results in an undesired non-uniformity in film thickness.

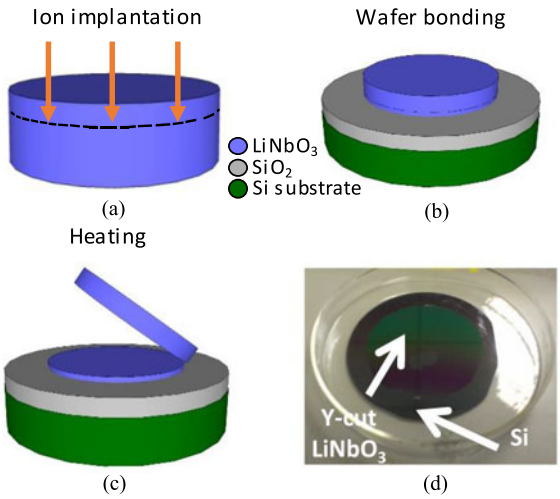

Fig. 3. (a)–(c) Summary of wafer-scale thin-film lithium niobate on silicon dioxide fabrication steps. The substrate can be silicon as shown here, or lithium niobate [72]. Reproduced with permission. Copyright 2017, John Wiley and Sons, Inc.; (d) A 3" thin film wafer of lithium niobate bonded to a 4" substrate wafer of oxidized silicon [73]. Reproduced with permission. Copyright 2013, The Optical Society.

2) Thermal Exfoliation: Following the initial success of CIS in forming free-standing films, a second method using thermal shock slicing or thermal exfoliation has been established for die-scale and wafer-scale bonding of thin films of LN on to different substrates (Fig. 1(b)–(d)). Thermal exfoliation is suitable for forming sub-micrometer-thick films, which are much thinner than the CIS films. The most successful approach using thermal exfoliation has been the direct bonding of thin-film LN on to silicon dioxide (SiO_2). This method resembles the Smart Cut process commercialized for silicon-on-insulator (SOI) wafers [69]. The first demonstrations of thin-film LN directly bonded to SiO_2 on LN substrates were die-scale [70]. Wafer-scale demonstrations soon followed [71]. Sometimes, these wafers are called lithium niobate on insulator (LNOI).

Arguably, the wafer-scale demonstration of thin film LN bonded to oxidized Si substrates is technologically more interesting. The advantages of silicon substrates over LN include cost, potential compatibility with silicon photonics, as well as relaxation of processing conditions of LN-based devices themselves. For example, the extremely low thermal conductivity of LN makes thermal cycling of the material challenging. Silicon substrates, in contrast, are very versatile and can easily handle thermal cycles. Also, processing issues associated with high levels of pyroelectric charges are diminished by eliminating bulk LN substrates.

Thin-film LN wafers on oxidized Si substrates were first reported by CREOL researchers in 2013 [73]. A major challenge that made this milestone elusive for years was the large thermal expansion coefficient mismatch between LN and Si, rendering the bonding of LN thin films at elevated temperatures infeasible. Progress in methods for room-temperature bonding has alleviated this issue. The wafer-scale fabrication steps for thin-film on Si substrates are summarized in Fig. 3. An ion-implanted LN donor wafer is bonded to a SiO_2 layer, which is thermally grown on Si substrate (in the aforementioned case of thin-film LN-on a SiO_2 buffer on LN substrates, plasma-enhanced chemical vapor deposition (PECVD) is typically used to deposit SiO_2 on the LN substrate). Next, the bonded wafers are annealed at 200 to 220 °C to thermally exfoliate the desired thin film of LN from the donor wafer. Similar to CIS, the high temperature annealing step here is crucial for recovering the EO and nonlinear properties of the LN thin film. Hence, after exfoliation, the temperature is increased to 400–500 °C to mitigate implantation-induced material degradation. Finally, the LN thin film surface is subjected to a chemical mechanical polish (CMP) to improve the surface quality of the film, yielding surface roughness <1 nm. The thickness of the SiO_2 layer, the depth of the ion implantation, and the thin film material polished away in the last step, are all independent parameters, offering excellent control over the final thicknesses of the LN thin film and the SiO_2 lower cladding.

A somewhat different approach uses benzocyclobutene (BCB) [74], [75] as a polymer adhesive for die-scale bonding instead of direct bonding to SiO_2. Chips of LN, cleaved from a donor LN wafer implanted with He ions, are bonded to BCB coated LN chips. The post-bond annealing is similar to that for direct bonding to SiO_2, however, the last step of the anneal is at a lower temperature of 300 °C [76], [77]. The anneal temperature is one downside of this approach. BCB limits the highest temperature of the post-bonding anneal, which is crucial for the recovery of the implantation induced material degradation, where higher temperatures are desirable. The reliability of polymer-bonding is another drawback. Thus, direct-bonding on SiO_2 layers is preferred, and most of the recent work on thin film LN uses SiO_2 as the lower cladding insulator.

3) Thin-Film Lithium Niobate Bonded on Top of SOI: Wafer-scale bonding of LN to silicon has been pursued since the late 1990s [78], [79], i.e., around the same time as CIS. About a decade later, thin film platelets of LN were bonded to SOI waveguides [80]–[83], bringing together LN-Si bonding and CIS (Fig. 1(e)). An ion-implanted LN wafer is heated to thermally-exfoliated platelets of thin-film LN and annealed. These platelets are then bonded, directly, or using BCB, on top of a SOI microring resonator, to form the hybrid Si-LN platform. More recently, centimeter-size thin films of LN on a LN substrate have been bonded to SOI dies singulated from patterned SOI wafers [84] (Fig. 4).

4) Silicon on Single-Crystalline LN Wafers: There are two approaches to forming the Si on LN platform of Fig. 1(f) [85]–[87]. The first method is based on bonding unpatterned SOI to bulk single crystalline LN [85], [86]. The substrate and the buried oxide of the SOI are etched away, leaving behind a layer of single-crystalline Si on LN. The second approach uses a direct deposition of amorphous Si on a LN substrate [87]. In either case, the higher refractive index of silicon provides optical confinement in the platform upon patterning.

5) Mechanical Thinning: To achieve the platform depicted Fig. 1(g), a combination of polymer adhesive bonding followed by mechanical polishing is employed [88]. Stripes are plasma etched onto a bulk single-crystalline LN wafer, which is then bonded, patterned side-down onto a Si wafer using an ultraviolet

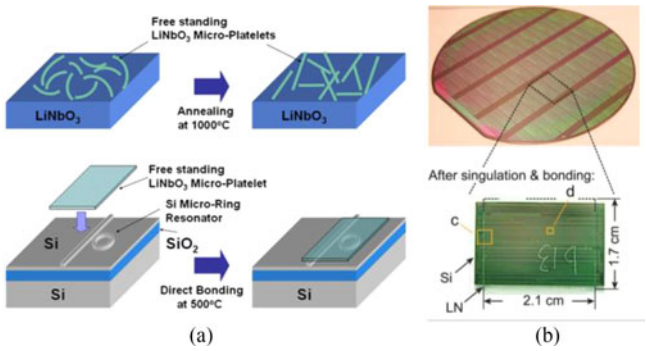

Fig. 4. (a) Summary of the bonding of thin-film LN on SOI [80]. Reproduced with permission. Copyright 2011, The Optical Society; (b) A picture of a LNOI die bonded to a SOI die. The transparent LN substrate of the thin film LN has not been removed [84]. Reproduced with permission. Copyright 2016, Nature Publishing Group.

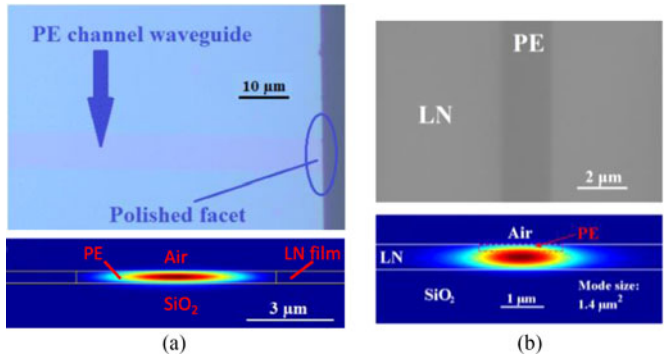

Fig. 5. Micrograph and scanning-electron-microscope image, along with the corresponding optical mode simulations, for (a) high loss [90], and (b) low loss [92], proton exchanged waveguides in thin film LN. The drastic reduction in PE area reduces the propagation loss. Reproduced with permission. Copyright 2015, The Optical Society.

(UV) curable adhesive layer. After curing, the LN substrate is mechanically thinned down, followed by tuning the thickness by dry etching, to form waveguides [88].

B. Waveguide Fabrication

In this section, some of the different approaches that have been pursued towards forming compact LN waveguides on the wafer platforms discussed above are reviewed.

1) Proton Exchange and Annealed Proton Exchange: The PE method is well-established for forming waveguides in bulk LN wafers [39], [40]. PE relies on the replacement of Li^+ ions in LN with hydrogen ions (H^+ or protons) to locally increase the extraordinary refractive index and provide optical confinement. PE results in the formation of a complex series of distinct crystallographic phases of the form $Li_{1-x}H_xNbO_3$. These phases are often accompanied by scattering loss, and degraded nonlinear and EO performance. When PE is followed by a controlled anneal, the process is called annealed proton exchange (APE) [41]. Annealing helps mitigate some of the undesired effects of PE [89]. Both PE and APE have been used to form waveguides in thin film LN [90], [91] with losses ranging from 11 dB/cm to 16 dB/cm for PE, and 0.6 dB/cm for APE. More recently, a very short PE time has been used to realize a small exchange depth [92], resulting in low loss waveguides (0.2 dB/cm) without a post-PE anneal (Fig. 5). These waveguides present micron-scale cross sections, at the cost of high bending radii, as discussed in Section IV.

2) Rib Loading: Arguably, the most straightforward way to form waveguides on a thin film of LN is to deposit a different dielectric or semiconductor on the thin film. The dielectric film is then patterned to form a rib, which loads the LN thin film. The refractive index of the rib-loading material should be closely matched that of LN to maximize the confined optical energy in the LN layer. This approach has been demonstrated using a handful of materials, such as tantalum pentoxide (Ta_2O_5) [73], [93], [94], titanium dioxide (TiO_2) [95], chalcogenide glass (ChG), e.g., $Ge_{23}Sb_7S_{70}$ [96]–[98], and silicon nitride (SiN) [99]–[102] (Fig. 6). The immediate benefit of rib-loading is the ease of processing, e.g., ChG and SiN are easier to etch than LN and offer

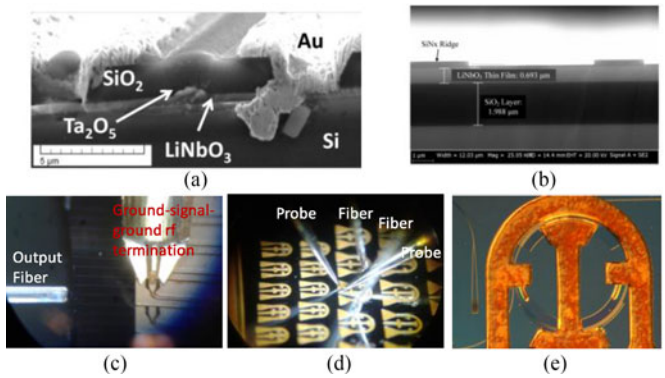

Fig. 6. Scanning electron microscope images of different rib-loaded thin-film LN waveguides using (a) tantalum pentoxide [73]. Reproduced with permission. Copyright 2015, The Optical Society; and (b) silicon nitride [102]. Reproduced with permission. Copyright 2016, IEEE. Micrographs of chalcogenide loaded (c) Mach-Zehnder and (d) microring modulators being tested [96]. Reproduced with permission. Copyright 2015, The Optical Society. (e) Detailed electrode structure and a grating coupler of a microring modulator from (d).

TABLE I
PROPAGATION LOSS OF RIB-LOADED WAVEGUIDES

Rib material	Loss (dB/cm)	
Tantalum pentoxide	5	[73]
Titanium dioxide	5.8	[95]
Chalcogenide glass	1.2	[97]
Silicon nitride	1	[99]–[101]
Silicon nitride	7	[102]

smooth etched sidewalls for low waveguide propagation loss. Another advantage is that rib-loading is applicable to any LN crystal cut. The reported propagation loss of rib-loaded thin-film LN waveguides is summarized in Table I.

3) Dry Etching: As mentioned, LN has traditionally been difficult to chemically dry-etch [103]. Isotropic wet etching is not compatible with forming small waveguide cross-sections. Alternatively, dry etching assisted by argon, and argon milling, have been extensively investigated for patterning LN in both bulk single-crystalline, as well as thin-film wafers (Fig. 7) [104], [105]. Historically, etched thin film LN waveguides have

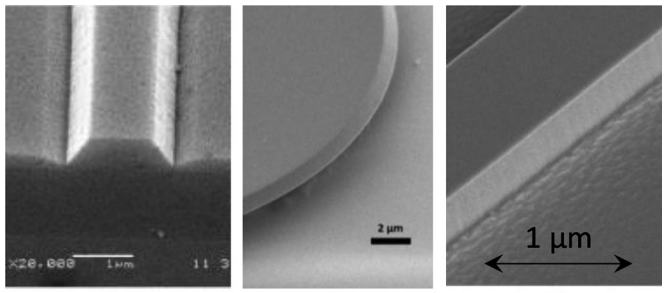

Fig. 7. Scanning-electron-microscope images of different argon-etched thin-film LN waveguide structures in chronological order of reporting: (a) [103]. Reproduced with permission, 2008; (b) [105]. Reproduced with permission. Copyright 2014, The Optical Society; and (c) [106]. Reproduced with permission, 2017. The improvement in sidewall roughness over time is evident, culminating in 0.4 dB/cm propagation loss demonstrated in (c).

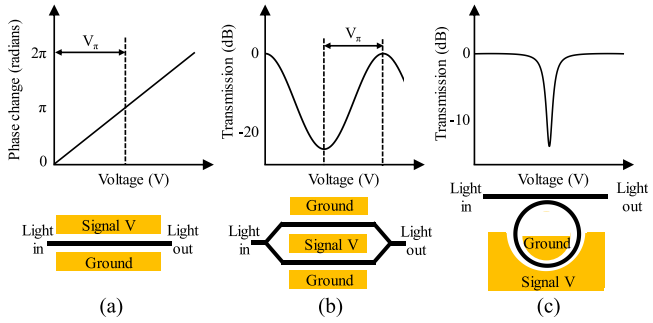

Fig. 8. Transfer functions for (a) phase, (b) Mach-Zehnder, and (c) microring modulators.

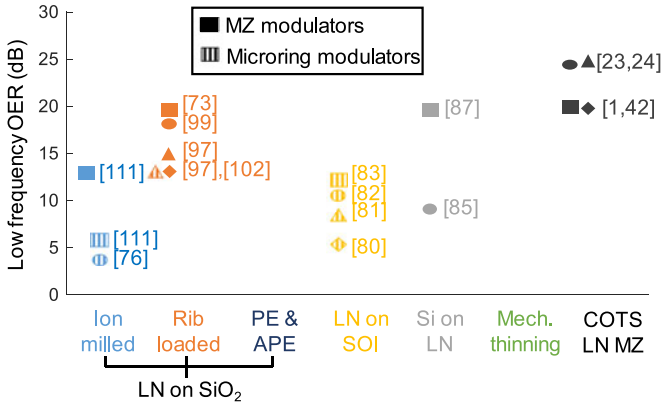

Fig. 9. Low-frequency optical extinction ratio for MZ and microring modulators. The OER for certain ring modulators, when not explicitly mentioned, has been extracted from voltage tuning measurements.

suffered from high propagation losses. In one recent demonstration, though, low-loss waveguides (0.4 dB/cm) have been realized [106]. However, this particular demonstration is only on *Z*-cut LN, where the re-deposition of material from the dry etching is expected to be different from *X*- and *Y*-cut. Nonetheless, this encouraging report on etching *Z*-cut LN is an important milestone towards realizing low-loss *X*- and *Y*-cut LN waveguides using dry etching.

4) Thin-Film Lithium Niobate Bonded on Top of SOI: There is no LN-related waveguide processing when forming waveguides by bonding LN thin films on top of SOI waveguides, i.e., the entire burden of waveguide formation is on the SOI end of the processing. SOI waveguides with thin film LN bonded on top with losses of 4.3 dB/cm have been reported [84]. Due to the high refractive index of Si compared to LN, bending radius is often sacrificed for optical mode overlap with the EO LN film.

5) Silicon on LN: The main feature of the silicon-on-LN platform (Fig. 1(f)) is the elimination of SiO_2 cladding layers. This is particularly advantageous in the mid-wave infrared wavelengths, where SiO_2 is optically lossy. Mid-infrared modulation (at 3.4 μm wavelength) has been demonstrated using crystalline Si thin films bonded on LN substrates [85]. The reported waveguide propagation loss is as ~2.5 dB/cm. Further processing optimization has led to 0.8 dB/cm in microrings [86]. Depositing amorphous Si on LN substrate is easier than bonding crystalline SOI and removing the substrate. The tradeoff is a higher propagation loss of ~3 dB/cm [87].

6) Mechanical Thinning and Other Methods: Modulators formed using mechanically-thinned LN waveguides adhesive-bonded to silicon (Fig. 1(g)) have reported waveguide losses ~1 dB/cm [88]. Other waveguide structuring methods, such as femtosecond laser writing [107] and optical grade dicing [108], are not discussed here, since have not been used to form modulators in thin film LN.

III. Performance of Thin Film LN EO Modulators

The performance of three types of electrooptic modulators, namely the phase, Mach-Zehnder (MZ), and microring types, shown in (Fig. 8), is discussed in this section.

A. Optical Extinction Ratio

The optical extinction ratio (OER) quantifies the optical power extinction offered by a modulator in the off state, relative to the on state at low frequencies (DC to a few MHz). The OER of a MZ and a microring modulator can be discerned as the ratio of the maximum to minimum value of the photoreceiver output. An ideal symmetric MZ modulator presents infinite OER. However, fabrication imperfections, such as deviations from 50:50 power splitting and combining, and loss-imbalance between the arms of the MZ modulator, lead to finite OERs. The OER for an EO microring modulator is determined by the passive spectral response of the microring, which in turn depends on the coupling coefficient between the bus waveguide and the microring, the propagation loss in the microring, and the excess loss at the coupler.

The specific application of the modulator determines the acceptable OER range. Above 20 dB OER is required for long-haul communications and over 30 dB is desirable in certain switching applications, while short-reach transmission can tolerate lower OER.

A summary of OER for thin-film LN EO modulators is presented in Fig. 9. This includes all the various platforms discussed in Section II, as well as COTS LN MZ modulators. Similar charts are shown for other figures of merits in the following sections.

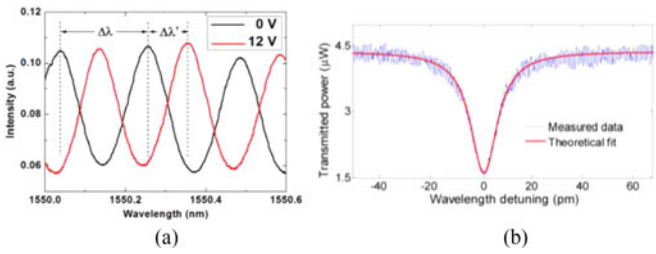

Fig. 10. (a) Fabry-Perot reflections of a thin-film LN phase modulator [110]. Reproduced with permission. Copyright 2016, The Optical Society; (b) Resonance of a microring modulator [97]. Reproduced with permission. Copyright 2015, The Optical Society. Theoretical fits to measured data for both (a) and (b) are sufficient to extract propagation loss.

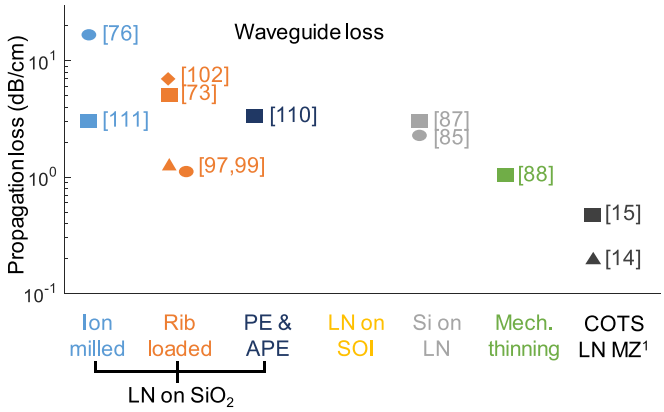

Fig. 11. Waveguide loss for different modulator demonstrations. Some microring modulator data is omitted because the loss in a microring is often increased, i.e., the quality factor is decreased, in order to increase modulation bandwidth. Thus, it is not indicative of the quality of the platform employed. [1]These loss values are on waveguides per se, not MZ modulators, but with processing conditions similar to those used in COTS modulators.

In all cases, an empty column signifies that the corresponding metric has not been reported for that particular platform. It is observed from Fig. 9 that, in the case of the OER, rib-loaded (Fig. 1(c)) and Si-on-LN (Fig. 1(f)) thin-film platforms offer the best performance and are on par with COTS LN modulators.

B. Optical Loss

Some loss values (propagation loss) were mentioned in Section II-B. Optical loss, an important metric, is reviewed and discussed here in more depth. The optical loss of a MZ modulator can be considered to have various contributions and associated parameters. The overall insertion loss of the interferometer is an important system parameter that depends on coupling loss and propagation loss. Coupling loss depends on the mode overlap between the input light field and the waveguide mode, and the quality of the waveguide facet. The propagation loss depends on material absorption, sidewall scattering induced loss, and metal induced absorption associated with the overlap of the edges of the optical mode with the metal electrodes. Another important component is the loss imbalance between the two MZ arms, which degrades the extinction ratio, and may affect the chirp. This includes scattering from undesired contaminants and fabrication defects.

Optical loss for a microring modulator can be split up similarly. The on-chip insertion loss here includes the propagation loss in the bus waveguide and in the microring region, as well as the less significant loss of the directional coupling region. Obviously, the propagation loss in the microring has a significant impact on the optical quality factor, i.e., it influences the limit of the modulation speed of the microring.

The optical loss of a straight waveguide, such as a phase modulator, can be extracted from Fabry-Perot reflections (Fig. 10(a)). Alternatively, microrings can be used as well (Fig. 10(b)). A summary of waveguide propagation losses of the variously discussed technologies is presented in Fig. 11. The data has been limited to demonstrations of modulators. The rib-loading platform (Fig. 1(b)) offers the lowest propagation loss of ~1 dB/cm among modulators, although it is still higher than the ~0.2 dB/cm values in COTS devices.

C. Half-wave Voltage and Tunability

The half-wave voltage, V_π, also called the switching voltage, is the voltage required to toggle a MZ modulator between the on and off states. For a phase modulator, it is the voltage required to accumulate a π-phase shift over the device length, L. The half-wave voltage-length product, $V_\pi L$, is a figure of merit that is often used to qualify the design of the MZ modulator, since it is independent of the device length, L. The tunability, in pm/V, is the analog of V_π for microring modulators, which represents the spectral shift of an optical resonance of the microring modulator per volt applied to the electrodes. The V_π and tunability determine which electrical drivers are suitable to drive a modulator, and whether amplifiers are necessary.

Fig. 12 summarizes the trend of V_π and $V_\pi L$ values among compact LN EO MZ modulators. The rib-loaded devices [73], [97], [99], [102] have the lowest V_π of <3 V, comparable to COTS MZ modulators, but with much shorter lengths. The ion-milled and the rib-loaded variations of the thin-film LN on SiO_2 lower cladding approach (either on LN or Si substrates) offer the lowest $V_\pi L$ to date on any LN-based technology. This is because the high optical confinement facilitates the placement of the bias electrodes in close proximity of each other without incurring metal-induced optical loss.

In comparison, the ion-milled devices in [111] have 42% lower $V_\pi L$ than the rib-loaded device in [99] (1.8 vs. 3.1 V.cm). This $V_\pi L$ reduction corresponds well with the 37% reduction in electrode gap (3.5 vs. 5.5 μm), which is trivial to implement in rib-loaded structures since both types of waveguides offer similar lateral confinement and bending loss, as discussed later (Fig. 19). It is not clear whether the aggressive electrode proximity in [111] may have contributed to the higher loss of 3 dB/cm vs. 1 dB/cm in [99] (Fig. 11). Fig. 13 similarly presents the tunability for microring modulators. In this case, the LN-on-SOI technology has demonstrated the best performance, most likely because of the Z-cut oriented thin film. No high-speed measurements have been carried out on these particular Z-cut devices to date, as follows.

D. Modulation Bandwidth and Frequency Response

The 3-dB electrical modulation bandwidth is the frequency at which the electrical response of a calibrated photodetector

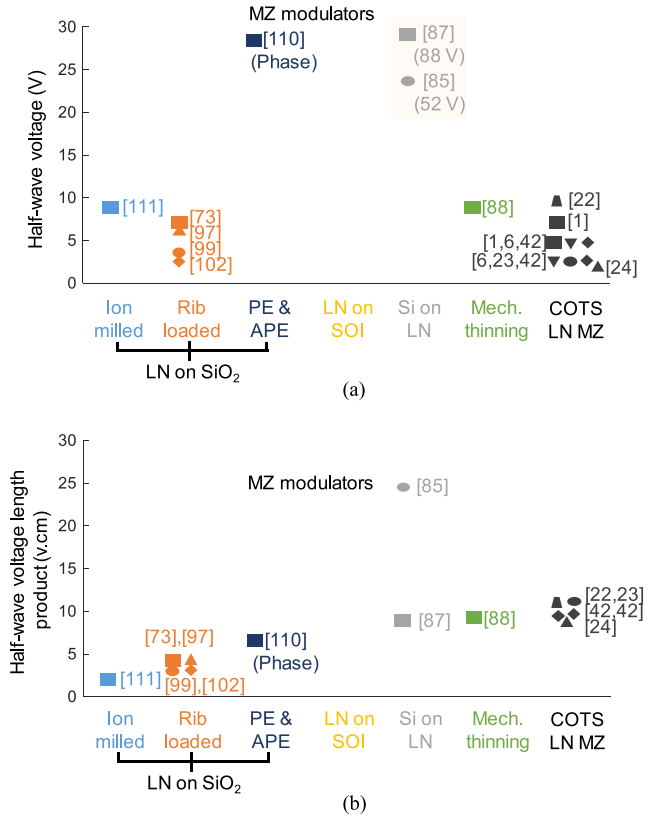

Fig. 12. (a) Half-wave voltage and (b) half-wave voltage length product of MZ modulators.

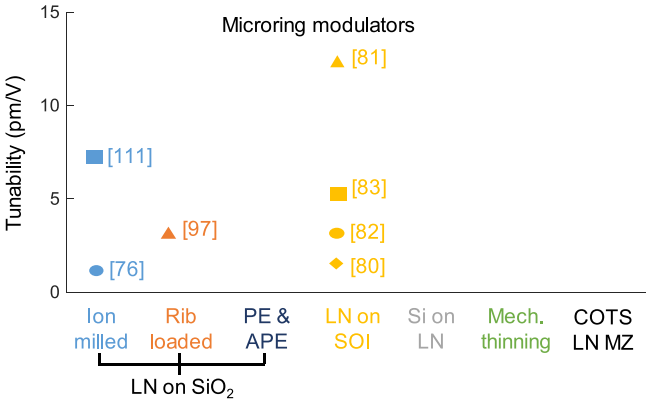

Fig. 13. Tunability of LN microring modulators.

(Fig. 14) measuring the modulated output wave drops to half of its low-frequency value. The frequency response is often complicated by acoustic waves in the LN waveguides and acoustic resonances in substrates, and clamping and unclamping of the LN structure, all of which lead to ripples, potentially larger than 1 dB, occurring at frequencies as large as a few GHz, depending on the physical structure. Fig. 15 tabulates the measured 3-dB bandwidths in various state-of-the-art devices. Among them, the SiN rib-loaded LN thin-film approach on Si substrate [99] has demonstrated the highest bandwidth of ~33 GHz to date. Design considerations for higher bandwidths are presented in Section IV.

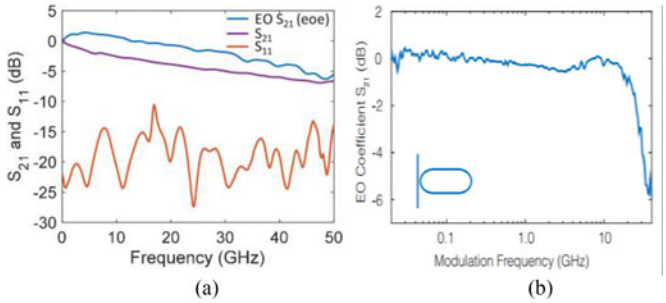

Fig. 14. Examples of frequency responses of compact LN EO modulators: (a) MZ type [99]. Reproduced with permission. Copyright 2016, The Optical Society; and (b) microring type [111]. Reproduced with permission.

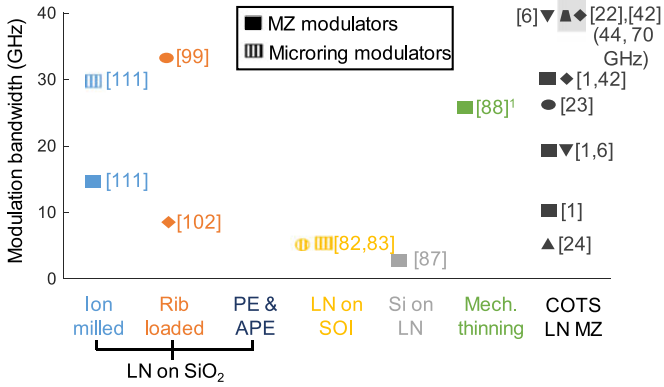

Fig. 15. 3-dB modulation bandwidth for both MZ and microring modulators.[1]

E. Digital Transmission

Digital data transmission has evolved into using a wide variety of higher order modulation formats [32], [33]. So far, however, thin film LN EO modulators have been used only for non-return to zero (NRZ) on-off keying (OOK), i.e., intensity modulation with direct detection. While higher order formats enable higher aggregate transmission bit rates for the same baud rate, the simplicity of detection for OOK makes it an attractive choice for data centers. We expect that higher order formats will be demonstrated on compact LN thin film modulators in the future.

Transmission rates for OOK in thin film LN EO modulators are presented in Fig. 16. Evidently, the reported data is sparse for these measurements. Also, since electrical extinction ratio, the length of the pseudorandom bit sequence used, and other factors are important for a complete picture of digital transmission, we refer the reader to the relevant references provided in the figure for further experimental details.

F. Linearity and Dynamic Range

The linearity of the transfer function of a modulator around a particular operating or bias point is central to the analog performance of the modulator. The nonlinear distortion present in an analog link is comprised of the nonlinearity of the modulator and the rest of the link (sources, amplifiers, detectors, RF spectrum analyzers, and any other components). The most

[1]Estimated from optical sideband measurements. This particular MZ modulator has been tested up to 110 GHz.

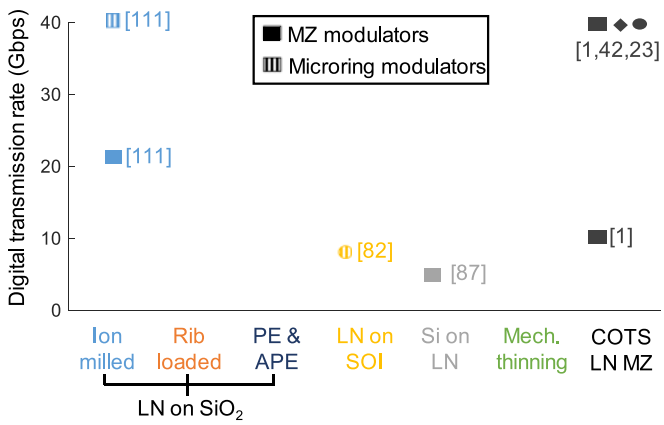

Fig. 16. Comparison of OOK data rates for various compact LN modulators.

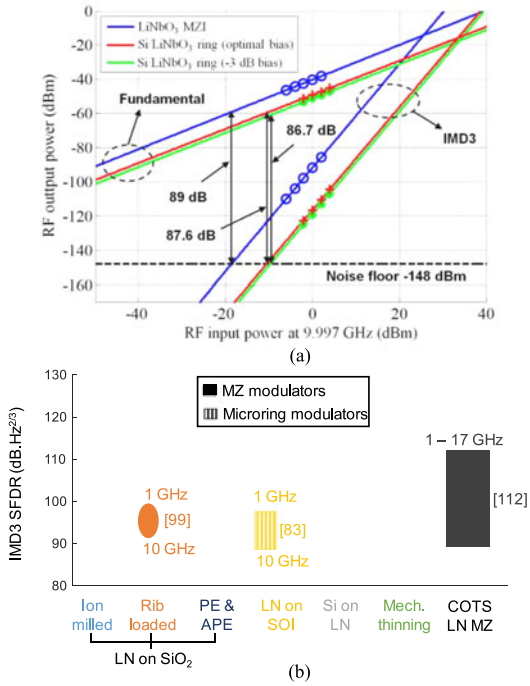

Fig. 17. (a) IMD3 measurements for a LN on SOI microring modulator, along with a benchmark COTS LN MZ modulator for comparison [81]; (b) IMD3 SFDR for compact LN EO modulators.

straightforward way to quantify the distortion is by measuring intermodulation products. For two in-band modulation tones of frequencies f_1 and f_2, the in-band intermodulation distortion (IMD) tones are usually the third-order intermodulation (IMD3) tones at $2f_1 - f_2$ and $2f_2 - f_1$. If the bandwidth is over an octave, second-order distortion tones, such as $f_1 + f_2, 2f_1$, and $2f_2$ become important. These effects are cubic and quadratic, respectively. The spurious-free dynamic range (SFDR) is the signal-to-noise ratio at the output at the frequency of a fundamental input RF tone when the IMD products are equal in power to the noise at the output, for a two-tone input of identical power.

A typical IMD3 measurement is shown in Fig. 17(a) [83], while a comparison of SFDR for compact LN EO modulators is shown in Fig. 17(b). There are only two reports in this regard for the novel compact structures reviewed here, with SFDRs in the 90 to 100 dB.Hz$^{2/3}$ range. Evidently, the performance of these early reports are comparable to the COTS counterparts.

It is noted that the SFDR of a modulator is only one of the many metrics required to evaluate an analog link. However, it is the only feature of the link which cannot be improved by amplification before and after the link. We refer the readers to excellent reviews on the linearity of analog links [112] and microwave photonics [113], [114].

IV. Design

The design of compact LN modulators is discussed here for *X*-cut thin-film LN modulators. Similar guidelines can be established for *Z*-cut modulators.

A. Waveguide and Low Frequency Design

As seen throughout this paper, there are many approaches that have been utilized to form waveguides for the modulators in thin film LN. In this section, rib-loaded, ion milled, and PE single-mode waveguides are analyzed. For the purposes of optical design, the approach of thin-film *X*-cut LN bonded on top of SOI (Fig. 1(e)) can be treated as a specific case of rib loading a thin film of LN, though from the bottom and with a non-index-matched material, i.e., Si. Similarly, waveguides formed by mechanical thinning are optically identical to ion-milled waveguides.

Assuming a longitudinally uniform structure, the low frequency V_π for a symmetric push-pull-configuration [99] MZ modulator is

$$V_\pi = \frac{\lambda n_{eff}}{\pi L n_e^4 \Gamma}, \tag{1}$$

where n_{eff} is the effective index of the waveguide mode and n_e is the extraordinary material index of LN. Γ is an overlap integral parameter given by

$$\Gamma = \frac{\iint \left[\frac{E(x,y)}{V}\right] r_{33}(x,y)\overrightarrow{E_1} \cdot \overrightarrow{E_1^*} dxdy}{\iint \overrightarrow{E_1} \cdot \overrightarrow{E_1^*} dxdy}, \tag{2}$$

where $E(x,y)/V$ is the RF frequency electric field per volt applied to the electrodes, and E_1 is the electric field of the optical mode. It is important to note that $E(x, y)/V$ has units of 1/length. For a pair of ideal parallel plates, it is the inverse of the separation between the plates. The integral in the numerator is performed only over the extent of the EO material (since $r_{33} = 0$, elsewhere), while the denominator is over the entire transverse cross section. V_π depends on the electric field per applied volt, and the overlap of the electric field with the intensity of the optical mode in the EO material–these can be tuned through optical and electrical design, as well as the device length.

Generally, well-confined compact optical modes are desirable. This is due to a number of reasons–they have, for instance, small bending radii, which enable dense photonic routing, essential for any large-scale integration. An immediate example is the reduction in the size of *Y*-junctions and microring modulator radii. Furthermore, the gap between the electrodes can

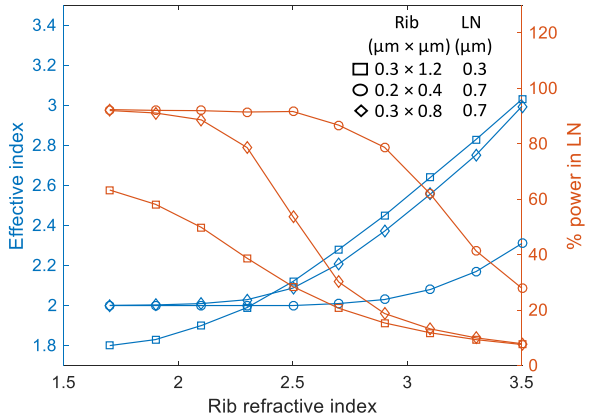

Fig. 18. Effect of the refractive index of the rib loading material on waveguide effective index and the modal power confinement in the LN slab, for the combination of rib (height × width) and LN (slab height) dimensions indicated in the legend.

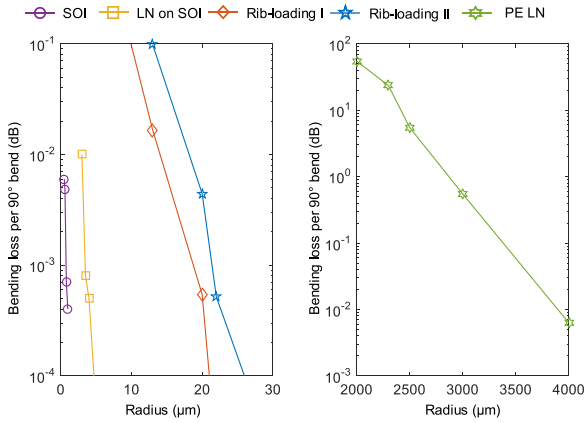

Fig. 19. Bending loss per 90° bend in dB for different platforms. SOI waveguides are shown as a benchmark. The LN-on-SOI waveguide presents the smallest bending losses, but only when ∼30% of the optical power is confined in the LN cladding film, while the rest is in the SOI waveguide core (data extracted from [84]). The two rib-loaded waveguides show bend radii below 20 μm when width of the rib material is varied between I (2.4 μm) and II (1.2 μm). The PE waveguides (shown separately) present high bending radii due to the small exchange depth used for obtaining low loss (data extracted from [92]).

be decreased as the confinement of the optical mode increases. This leads to a reduction in V_π, evident in (1).

Fig. 18 shows the variation of the effective index of the fundamental transverse-electric (TE) mode with the index of the rib loading material. The physical dimensions are indicated in the legend of Fig. 18, and the simulations were carried out using an eigenmode solver (COMSOL). While practical aforementioned examples include Ta_2O_5, ChG glass, SiN, and Si, the entire range of indices from 1.44 (SiO_2) to 3.48 (Si) can, in principle, be covered using plasma-enhanced chemical vapor deposition of silicon oxynitride, SiN, silicon rich SiN, and amorphous Si. The theoretical discussion here is limited to practical indices, ranging from 1.7 to 3.5.

Control over the optical effective index is a crucial aspect of velocity matching for RF design, discussed later. At the same time, the fraction of the intensity of the optical mode in the LN (Fig. 18) also affects the V_π. It is evident that, the aforementioned issues of etching LN and propagation loss notwithstanding, ion-milled LN and PE waveguides offer less control over the effective index, limited by the material refractive index. However, over 95% of the light is confined in LN in these cases.

Bending losses are simulated using eigenmode simulations in COMSOL. The loss per 90° bend is tabulated in Fig. 19 for waveguide structures representative of LN on SOI, rib-loaded, and PE-LN. The LN-on-SOI waveguide exhibits low bending loss for ∼5 μm bending radius, but sacrifices modal overlap with the electrooptically-active LN top cladding (∼30% overlap). The rib-loaded structure is similar to those of Fig. 18 with a 300-nm-thick LN slab and a rib index of 2.2. Ion-milled waveguides (not shown) present bending loss similar to rib-loaded waveguides for the same bending radius and LN slab thickness. The rib-loaded waveguides show both small effective areas and tight bending radii. The PE waveguides clearly offer small waveguide areas, and have demonstrated low propagation losses, but they have very high bending radii. The data for LN on SOI and PE-LN can be found in [84] and [110], respectively.

Next, there is an inherent tradeoff between metal-induced propagation loss and the V_π, mediated by the electrode gap and the optical confinement. The more tightly-confined the waveguide, the smaller the electrode gap, the higher the electric field per applied volt, and the lower the V_π. However, any further narrowing of the electrode gap after a certain value leads to significant metal-induced optical loss. This critical electrode gap depends on the particular waveguide structure under consideration.

The variation of the average electric field per applied volt is shown in Fig. 20. The electric field is averaged over two areas: the area of the rib, and the LN slab area under the rib, which is a good approximation for the well-confined waveguides of interest. Clearly, the RF electric field per applied volt drops sharply, in both the rib and the LN slab, as the dielectric constant, ε, of the rib increases. This can be understood through elementary electromagnetic boundary conditions. However, the consequence of this constraint is that the dielectric constant of the rib material strongly affects the overall V_π. This adverse impact on V_π is very strong for the case of a LN rib (i.e., ion-milled waveguide), as compared to rib materials with lower RF dielectric constants (e.g., SiN). In other words, depending on the refractive indices and mode distribution, the drop of the field per volt associated with the very high RF dielectric constant of a LN rib plays against the higher optical mode overlap with the EO-active material it offers.

Finally, it is important to note that the electrode-induced loss can be used in microring modulators to tune the quality factor and therefore the maximum modulation frequency. This illustrates an additional perspective on the loss-tuning tradeoff compared to the loss-V_π tradeoff. Also noteworthy is that the full optimization of the V_π may also be affected by the RF design discussed in the following section.

Before delving into the RF design for MZ modulators, additional requirements for microring modulators are briefly discussed. With small dimensions, microring electrodes can be treated as lumped elements driven as capacitors. The

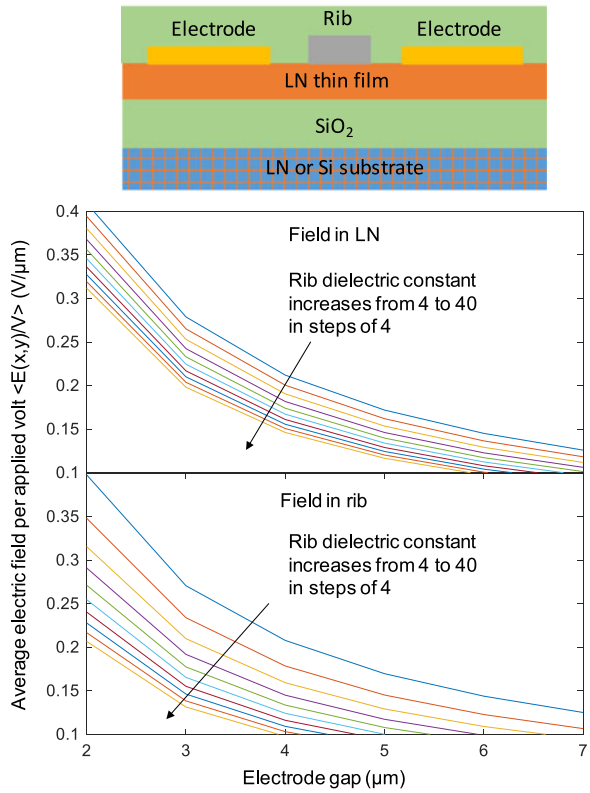

Fig. 20. Average electric field per applied volt as a function of electrode gap and rib dielectric constant for the structure shown above. The top plot presents the average field in LN and the lower plot is the corresponding value in the rib. Depending on the rib index, electrode gaps as low as 3 μm present prohibitively high propagation loss.

modulation bandwidth is limited by the product of the capacitance (C) and total resistance (R). Accordingly, a simplified model for the RF half-wave voltage is

$$V_\pi(\omega) = V_\pi(0)\left[1 + i\omega RC\right], \tag{3}$$

where $V_\pi(0)$ is the half-wave voltage at DC. A detailed treatment of microring modulators can be found in [115].

B. RF Design

There are many facets to the RF design of traveling-wave electrodes of MZ modulators, which must be managed simultaneously with low frequency and waveguide design. The optical modulation frequency response, $m(f)$, is [116], [117]

$$m(f) = \left| \frac{(\Phi_+ + \Gamma_L \Phi_-)(1 + \Gamma_S)}{\exp(2i\Phi_+) + \Gamma_L \Gamma_S \exp(-2i\Phi_-)} \right|, \tag{4a}$$

$$\Phi_\pm = \exp(iu_\pm)\sin(u_\pm)/u_\pm, \tag{4b}$$

$$u_\pm = \pi(n_{RF} \mp n_{opt}) fL/c - i\alpha_{RF} L/2, \tag{4c}$$

$$\Gamma_L = (Z_L - Z_0)/(Z_L + Z_0); \Gamma_S = (Z_0 - Z_S)/(Z_0 + Z_S), \tag{4d}$$

where n_{RF} and n_{opt} are the RF and optical mode indices, respectively, f is the RF frequency, α_{RF} is the RF loss, Z_L and Z_S are the load (termination) and source impedances, respectively, and Z_0 is the characteristic impedance of the RF electrodes. $m(f)$ quantifies the optical frequency response of the modulator. Γ_L and Γ_S are the RF reflections between the termination and the electrodes, and the electrodes and the source, respectively. The 3-dB electrical bandwidth can be estimated from the $[m(f)]^2 = 1/2$ condition.

There are a number of design considerations for high-speed design–velocity matching, impedance matching, and RF loss. Velocity matching is the propagation effective-index mismatch between the RF and optical fields, contained in the $u_\pm$ terms. The smaller the difference of n_{RF} and n_{opt}, the higher the modulation bandwidth. The Z_L and Z_S impedances are typically 50 Ω. Though frequency-dependent, the characteristic impedance of the electrodes is then designed to be as close to 50 Ω as possible, to minimize electrical reflections at the RF input and from the terminating impedance. Finally, the RF loss can be decomposed into a sum of metal and dielectric loss. The higher the RF loss, the lower the modulation bandwidth.

The RF electrode design comprises of a fine balance between the above three factors in conjunction with the limitations imposed by the aforementioned low-frequency and waveguide design considerations. The RF index and characteristic impedance can be modeled by finite element and boundary element methods, among others.

An immediate benefit of using thin-film LN is that velocity matching is much more straightforward than in COTS low-index-contrast counterparts. LN has a much higher RF dielectric constant than the square of its optical index, resulting in a much higher n_{RF} compared to n_{opt}. COTS LN MZs have managed to work around this by techniques such as using SiO_2 buffer layers and very thick electrodes to shift the RF mode upwards. However, this consideration is diminished significantly for thin film LN because of the reduced thickness of LN and the lower dielectric constant of the surrounding SiO_2 ($\varepsilon \sim 3.9$). Thus, the thin film LN electrodes can be $\sim$1 μm tall, unlike the $\sim$10 μm or more for COTS MZ modulators.

In the limit of negligible RF reflections (i.e., good impedance matching), the modulation response is simplified to [118]

$$m(f) = \exp\left(-\alpha_0 \sqrt{f} L/2\right) \left[\frac{\sinh^2\left(\frac{\alpha_0 \sqrt{f} L}{2}\right) + \sin^2\left(\pi v f L\right)}{\left(\frac{\alpha_0 \sqrt{f} L}{2}\right)^2 + \left(\pi v f L\right)^2} \right]^{1/2}, \tag{5}$$

where $v = (n_{RF} - n_{opt})/c$ is the velocity mismatch, and α_0 is the metal RF loss parameter at 1 GHz.

This latter form lends itself to easier analysis than (4). The reduced modulation with increasing RF loss and velocity mismatch is evident in (5). The velocity mismatch has a sinusoidal contribution to the numerator and a quadratic contribution to the denominator. The RF loss scales as a decaying exponential in the numerator, and a quadratic in the denominator. Equation (5) has been used to quantify the bandwidth-length tradeoff [118], i.e., the decrease in RF bandwidth with increasing device length. This is clear in (5), where the effects of velocity mismatch and RF loss are both scaled by the device length. Thus, an increase in any of v, α_0, and L will diminish the modulation and hence the bandwidth.

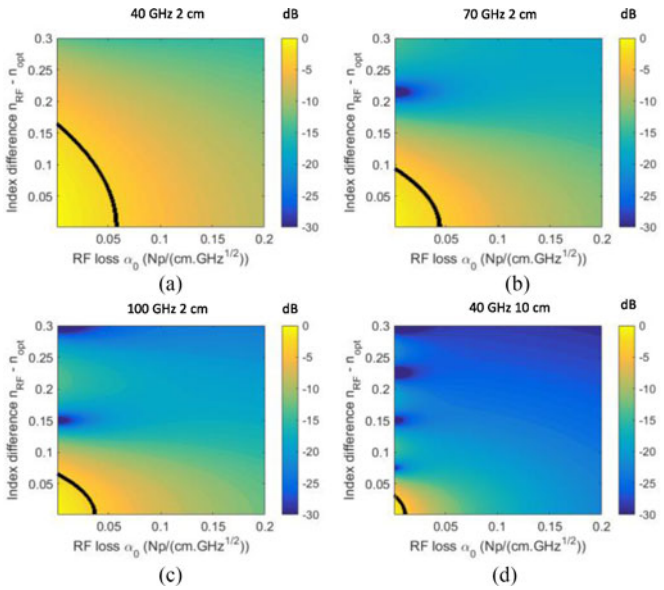

Fig. 21. EO S_{21} roll-off in dB for a range of velocity mismatch and RF loss for the following pairs of frequency and electrode length (a) 40 GHz and 2 cm; (b) 70 GHz and 2 cm; (c) 100 GHz and 2 cm; (d) 40 GHz and 10 cm. The 3-dB modulation bandwidth is marked with a black contour line in each plot.

Here, general design guidelines for velocity mismatch and metal RF loss in the presence of good impedance matching are established. The EO S_{21} roll-off is plotted in Fig. 21(a)–(c) at frequencies of 40, 70, and 100 GHz for 2-cm-long electrodes. Fig. 21(d) provides a benchmark at 40 GHz and 10 cm. The two lengths are chosen to facilitate a comparison between shorter thin-film and longer COTS LN MZ modulator, when both are set up for a DC V_π of 1 V. Evidently, the compact devices can yield much higher modulation bandwidths with comparatively relaxed design tolerances, even up to 100 GHz, for low voltage operation.

V. Outlook

As reviewed in Section III, the performance of compact thin film LN modulators is now on par with COTS LN MZ modulators in several key figures of merit. 3-dB modulation bandwidths up to 33 GHz [99] and operation up to 110 GHz [88] have been independently confirmed in MZ modulators, along with 30 GHz bandwidth in microring modulators [111]. In addition, low switching voltages and good extinction ratios have been established. Potential applications of this emerging technology include communications in optical interconnects, terrestrial and submarine systems, RF-photonics, millimeter wave imaging, and electric field sensing. However, there are some milestones on the road to commercial viability that have yet to be achieved.

The first milestone is packaging. The compact modulator demonstrations so far have yet to be equipped with optical and RF packaging. RF-compliant packaging has the challenge of not perturbing the modulator response and is a complicated task. Furthermore, perhaps all demonstrations so far have utilized some form of optical alignment stages for optical coupling. Such systems may be susceptible to drift over time. This has obviated the study of thermal drift, DC drift and reliability. These are crucial aspects of modulator performance for real-world deployment. It is expected that work on these fronts will come to fruition soon.

There is further device optimization to look forward to. As established in Section IV-B, the design requirements for achieving 100 GHz modulation bandwidth at low switching voltages ($\sim$1 V) are well within those of COTS LN modulators. It is expected that such high- and low-power devices will be realized in the near future.

In the meantime, there are many exciting possibilities heralded by the realization of compact LN modulators. Perhaps the most exciting commercial application is expected to be in data centers and high-performance-computing. With the ever-increasing data rate requirements, the use of on-off keying and direct detection in these infrastructures will likely be replaced by the use of higher-order modulation formats, aided by forward-error correction and other digital signal processing techniques. There is room for growth across the entire spectrum of core-to-core to inter-data-center interconnects. In a similar vein, metro- and long-haul-terrestrial and submarine telecommunication may evolve into using denser WDM grids, potentially aided by frequency combs, to address increasing data rates. Higher-order modulation formats and coherent detection might be employed up to certain transmission lengths. Compact thin-film LN modulators are indeed promising candidates for such applications. Their small footprint renders them attractive for high-density on-chip integration. Their high extinction ratio, compared to the other modern compact modulators mentioned in Section I, is attractive as well for all the above applications. They also have potential applications in forming miniaturized compact ultrafast versions of the LN optical switches demonstrated around the 1990s and onwards.

With the anticipated improvements in linearity, compact LN modulators are promising candidates for analog links. RF-photonic down converting links have recently been demonstrated in-flight [119]. The adoption of optical-fiber-based interfacing in an aircraft can potentially lead to significant weight reduction by eliminating coaxial cables. Similar considerations apply to naval vessels.

Millimeter waves offer tremendous potential for imaging applications, based on their penetration through smoke, fog and clouds. There has been good progress in millimeter-wave beam formation and imaging using LN modulators [120]. Fully integrated implementations of these systems in the future may benefit in efficiency and sensitivity enhancements from the low switching voltages and high bandwidths that are anticipated of compact LN modulators. Along these lines, compact LN devices have already been utilized as compact electric field sensors [121], and there is room left in device optimization for better performance. Compact high-sensitivity electric field sensors may be exploited in medical applications, as a part of point-of-care monitoring systems, and in electromagnetic field sensing for the armed services. Finally and on a completely different note, compact LN MZ modulators have been investigated at visible wavelengths [122], potentially for the on-chip control of trapped ions.

VI. Conclusion

The technology of compact LN modulators has matured tremendously over the last several years and is becoming well -established for numerous applications, both, in the near future, and, in the long term. These devices, which are miniaturized versions of commercial-off-the-shelf LN modulators, can be densely integrated on silicon with low switching voltages and promising digital and analog performances. With advances in packaging and reliability studies, these devices may soon evolve into a formidable contender for a variety of evolving applications in data centers, high performance computing, digital and analog telecommunication links, sensors, and imaging, among others.

References

[1] [Online]. Available: https://www.thorlabs.com/newgrouppage9.cfm?objectgroup_id=3918

[2] [Online]. Available: https://www.thorlabs.com/newgrouppage9.cfm?objectgroup_id=3948.

[3] [Online]. Available: http://www.oclaro.com/product/400g-lithium-niobate-modulator/

[4] [Online]. Available: https://photonics.ixblue.com/products-and-applications/lithium-niobate-electro-optic-modulator

[5] [Online]. Available: https://www.lumentum.com/en/optical-communications/products/transmission-components-and-modules/modulators

[6] [Online]. Available: http://www.eospace.com/

[7] M. Izutsu, Y. Yamane, and T. Sueta, "Broad-band traveling-wave modulator using a $LiNbO_3$ optical waveguide," *IEEE J. Quantum Electron.*, vol. QE-13, no. 4, pp. 287–290, Apr. 1977.

[8] F. J. Leonberger, "High-speed operation of $LiNbO_3$ electrooptic interferometric waveguide modulators," *Opt. Lett.*, vol. 5, no. 7, pp. 312–314, Jul. 1980.

[9] R. E. Tench *et al.*, "Performance evaluation of waveguide phase modulators for coherent systems at 1.3 and 1.5 microns," *J. Lightw. Technol.*, vol. LT-5, no. 4, pp. 492–501, Apr. 1987.

[10] D. J. Blumenthal, P. R. Prucnal, L. Thylen, and P. Granestrand, "Performance of and 8×8 $LiNbO_3$ switch matrix as a gigahertz self-routing switching node," *Electron. Lett.*, vol. 23, no. 25, pp. 1359–1360, Dec. 1987.

[11] I. Sawaki *et al.*, "Rectangularly configured 4×4 Ti: $LiNbO_3$ matrix switch with low drive voltage," *IEEE J. Sel. Commun.*, vol. 6, no. 7, pp. 1267–1272, Aug. 1988.

[12] H. Nishimoto, M. Iwasaki, S. Suzuki, and M. Konodo, "Polarization independent $LiNbO_3$ 8×8 matrix switch," *IEEE Photon. Technol. Lett.*, vol. 2, no. 9, pp. 634–636, Sep. 1990.

[13] M. Fukuma, J. Noda, and H. Iwasaki, "Optical properties in titanium-diffused LiNbO3 strip waveguides," *J. Appl. Phys.*, vol. 49, no. 7, pp. 3693–3698, Jul. 1978.

[14] T. Nozawa, K. Noguchi, H. Miyazawa, and K. Kawano, "Water vapor effects on optical characteristics in Ti:$LiNbO_3$ channel waveguides," *Appl. Opt.*, vol. 30, no. 9, pp. 1085–1089, Mar. 1991.

[15] M. Fukuma and J. Noda, "Optical properties of titanium-diffused $LiNbO_3$ strip waveguides and their coupling-to-a-fiber characteristics," *Appl. Opt.*, vol. 19, no. 4, pp. 591–597, Feb. 1980.

[16] R. C. Alferness, L. L. Buhl, and M. D. Divino, "Low-loss fiber-coupled waveguide directional coupler modulator," *Electron. Lett.*, vol. 18, no. 12, pp. 490–491, Jun. 1982.

[17] V. Ramaswamy, R. C. Alferness, and M. Divino, "High efficiency single-mode fibre to Ti:$LiNbO_3$ waveguide coupling," *Electron. Lett.*, vol. 18, no. 1, pp. 30–31, Jan. 1982.

[18] I. Sawaki, H. Nakajima, M. Seino, and K. Asama, "Thermally stabilized z-cut Ti:$LiNbO_3$ waveguide switch," in *Proc. Conf. Lasers Electro-Opt.*, Washington, DC, USA, 1986, pp. 46–47.

[19] M. Seino *et al.*, "A low DC-drift Ti:$LiNbO_3$ modulator assured over 15 years," in *Proc. Opt. Fiber Commun. Conf.*, San Jose, CA, USA, 1992, pp. 325–328.

[20] H. Nagata, "DC drift failure rate estimation on 10 Gb/s X-cut lithium niobate modulators," *IEEE Photon. Technol. Lett.*, vol. 12, no. 11, pp. 1477–1479, Nov. 2000.

[21] M. Seino *et al.*, "20-GHz 3 dB bandwidth Ti:$LiNbO_3$ Mach-Zehnder modulator," in *Proc. 16th Eur. Conf. Opt. Commun.*, Amsterdam, The Netherlands, 1990, vol. PD3, pp. 999–1002.

[22] D. Dofli and T. R. Ranganath, "50 GHz velocity-matched, broad wavelength LiNbO3 modulator with multimode active section," *Electron. Lett.*, vol. 28, no. 13, pp. 1197–1198, Jun. 1992.

[23] J. Kondo *et al.*, "40-Gb/s X-Cut $LiNbO_3$ optical modulator with two-step back-slot structure," *J. Lightw. Technol.*, vol. 20, no. 12, pp. 2110–2114, Dec. 2002.

[24] M. M. Howerton, R. P. Moeller, A. S. Greenblatt, and R. Krahenbuhl, "Fully packaged, broad-band $LiNbO_3$ modulator with low drive voltage," *IEEE Photon. Technol. Lett.*, vol. 12, no. 7, pp. 792–794, Jul. 2000.

[25] K. Noguchi, H. Miyazawa, and O. Mitomi, "Frequency-dependent propagation characteristics of a coplanar waveguide electrode on a 100-GHz-Ti:$LiNbO_3$ optical modulator," *Electron. Lett.*, vol. 34, no. 7, pp. 661–662, Apr. 1998.

[26] N. Edagawa, K. Mochizuki, and H. Wakabayashi, "1.2 Gbit/s 218 km transmission experiment using in-line Er-doped optical fiber amplifier," *Electron. Lett.*, vol. 25, no. 5, pp. 363–365, Mar. 1989.

[27] T. Kataoka, Y. Miyamoto, K. Hagimoto, and K. Noguchi, "20 Gbit/s long span transmission experiments using a 270 photon/bit optical preamplifier receiver," *Electron. Lett.*, vol. 30, no. 9, pp. 715–716, Apr. 1994.

[28] K. Hagimoto *et al.*, "Limitations and challenges of single-carrier full 40-Gbit/s repeater system based on optical equalization and new circuit design," in *Proc. Conf. Opt. Fiber Commun., OFC 97*, Dallas, TX, USA, 1997, vol. ThC1, pp. 242–243.

[29] O. E. Delange, "Wideband optical communication systems Part II—Frequency division multiplexing," *Proc. IEEE*, vol. PROC-58, no. 10, pp. 1683–1690, Oct. 1970.

[30] N. A. Olsson *et al.*, "68.3 km transmission with 1.37 Tbit/s capacity using wavelength division multiplexing of ten single-frequency lasers at 1.5 μm," *Electron. Lett.*, vol. 21, no. 3, pp. 105–106, Jan. 1985.

[31] C. A. Brackett, "Dense wavelength division multiplexing networks: Principles and applications," *IEEE J. Sel. Areas Commun.*, vol. 8, no. 6, pp. 948–964, Aug. 1990.

[32] P. J. Winzer and R.-J. Essiambre, "Advanced optical modulation formats," *Proc. IEEE*, vol. 94, no. 5, pp. 952–985, May 2006.

[33] P. J. Winzer and R.-J. Essiambre, "Advanced modulation formats for high-capacity optical transport networks," *J. Lightw. Technol.*, vol. 24, no. 12, pp. 4711–4728, Dec. 2006.

[34] C. Kachris and I. Tomkos, "A survey on optical interconnects for data centers," *IEEE Commun. Surv. Tuts.*, vol. 14, no. 4, pp. 1021–1036, Oct–Dec. 2012.

[35] C. Kachris, K. Bergman, and I. Tomkos, *Optical Interconnects for Future Data Center Networks*. New York, NY, USA: Springer, 2013.

[36] A. Chakravarty, K. Schmidtke, S. Giridharan, J. Huang, and V. Zeng, "100G CWDM4 SMF Optical Interconnects for Facebook Data Centers," in *Proc. Conf. Lasers Electro-Opt.*, 2016, Paper STu4G.1.

[37] D. A. B. Miller, "Rationale and challenges for optical interconnects to electronic chips," *Proc. IEEE*, vol. 88, no. 6, 728–749, Jun. 2000.

[38] D. A. B. Miller, "Device requirements for optical interconnects to silicon chips," *Proc. IEEE*, vol. 97, no. 7, pp. 1166–1185, Jul. 2009.

[39] J. L. Jackel, C. E. Rice, and J. J. Veselka, "Proton exchange for high-index waveguides in $LiNbO_3$," *Appl. Phys. Lett.*, vol. 41, no. 7, pp. 607–608, Oct. 1982.

[40] P. G. Suchoski, T. K. Findakly, and F. J. Leonberger, "Stable low-loss proton-exchanged $LiNbO_3$ waveguide devices with no electro-optic degradation," *Opt. Lett.*, vol. 13, no. 11, pp. 1050–1052, Nov. 1988.

[41] M. L. Bortz and M. M. Fejer, "Annealed proton-exchanged LiNbO3 waveguides," *Opt. Lett.*, vol. 16, no. 23, pp. 1844–1846, Dec. 1991.

[42] K. Noguchi, O. Mitomi, and H. Miyazawa, "Millimeter-wave Ti:$LiNbO_3$ optical modulators," *J. Lightw. Technol.*, vol. 16, no. 4, pp. 615–619, Apr. 1998.

[43] R. F. Tavlykaev, K. Kueckelhaus, and E. I. Voges, "Index profile reconstruction of Ti:$LiNbO_3$ structures and bending loss evaluation from near-field measurements," *Proc. SPIE*, vol. 2150, pp. 263–270, May 1994.

[44] E. L. Wooten *et al.*, "A review of lithium niobate modulators for fiber-optic communications systems," *IEEE J. Sel. Topics Quantum Electron.*, vol. 6, no. 1, pp. 69–82, Jan. 2000.

[45] R. A. Soref and B. R. Bennett, "Electrooptical effects in silicon," *IEEE J. Quantum Electron.*, vol. QE-23, no. 1, pp. 123–129, Jan. 1987.

[46] G. T. Reed, G. Mashanovich, F. Y. Gardes, and D. J. Thomson, "Silicon optical modulators," *Nat. Photon.*, vol. 4, pp. 518–526, Aug. 2010.

[47] B. Jalali and S. Fathpour, "Silicon photonics," *J. Lightw. Technol.*, vol. 24, no. 12, pp. 4600–4615, Dec. 2006.

[48] G. Mak, C. Rolland, K. E. Fox, and V. Blaauw, "High-speed InGaAsP-InP electroabsorption modulators with bandwidth in excess of 20 GHz," *IEEE Photon. Technol. Lett.*, vol. 2, no. 10, pp. 730–733, Oct. 1990.

[49] S. Irmscher, R. Lewén, and U. Eriksson, "InP–InGaAsP high-speed traveling-wave electroabsorption modulators with integrated termination resistors," *IEEE Photon. Technol. Lett.*, vol. 14, no. 7, pp. 923–925, Jul. 2002.

[50] T. H. Wu, Y. J. Chiu, and F. Z. Lin, "High-speed (60 GHz) and low-voltage-driving electroabsorption modulator using two-consecutive-steps selective-undercut-wet-etching waveguide," *IEEE Photon. Technol. Lett.*, vol. 20, no. 14, pp. 1261–1263, Jul. 2008.

[51] O. Qasaimeh, P. Bhattacharya, and E. T. Croke, "SiGe-Si quantum-well electroabsorption modulators," *IEEE Photon. Technol. Lett.*, vol. 10, no. 6, pp. 807–809, Jun. 1998.

[52] J. Liu *et al.*, "Waveguide-integrated ultralow-energy GeSi electro-absorption modulators," *Nat. Photon.*, vol. 2, pp. 433–437, Jul. 2008.

[53] Y. Tang, J. D. Peters, and J. E. Bowers, "Over 67 GHz bandwidth hybrid silicon electroabsorption modulator with asymmetric segmented electrode for 1.3 μm transmission," *Opt. Express*, vol. 20, no. 10, pp. 11529–11535, May 2012.

[54] L. Alloatti *et al.*, "100 GHz silicon–organic hybrid modulator," *Light Sci. Appl.*, vol. 3, no. 5, Mar. 2014, Art. no. e173.

[55] M. Lauermann *et al.*, "40 GBd 16QAM Signaling at 160 Gb/s in a silicon-organic hybrid modulator," *J. Lightw. Technol.*, vol. 33, no. 6, pp. 1210–1216, Mar. 2015.

[56] J. Liu, G. Xu, F. Liu, I. Kityk, and Z. Zhen, "Recent advances in polymer electro-optic modulators," *RSC Adv*., vol. 5, no. 21, pp. 15784–15794, Jan. 2015.

[57] T. Baba *et al.*, "50-Gb/s ring-resonator-based silicon modulator," *Opt. Express*, vol. 21, no. 10, pp. 11869–11876, May 2013.

[58] Y. Yang *et al.*, "High-efficiency Si optical modulator using Cu travelling-wave electrode," *Opt. Express*, vol. 22, no. 24, pp. 29978–29985, Dec. 2014.

[59] A. M. Gutierrez *et al.*, "High linear ring-assisted MZI electro-optic silicon modulators suitable for radio-over-fiber applications," in *Proc. IEEE 9th Int. Conf. Group IV Photon.*, 2012, pp. 57–59.

[60] Y. Tang *et al.*, "50 Gb/s hybrid silicon traveling-wave electroabsorption modulator," *Opt. Express*, vol. 19, no. 7, pp. 5811–5816, Mar. 2011.

[61] M. Lauermann *et al.*, "Generation of 64 GBd 4ASK signals using a silicon-organic hybrid modulator at 80 °C," *Opt. Express*, vol. 24, no. 9, pp. 9389–9396, May 2016.

[62] F. Gitmans, Z. Sitar, and P. Günter, "Growth of tantalum oxide and lithium tantalate thin films by molecular beam epitaxy," *Vacuum*, vol. 46, nos. 8–10, pp. 939–942, Aug.–Oct. 1995.

[63] Y. Nakata, S. Gunji, T. Okada, and M. Maeda, "Fabrication of $LiNbO_3$ thin films by pulsed laser deposition and investigation of nonlinear properties," *Appl. Phys. A*, vol. 79, nos. 4–6, pp. 1279–1282, Sep. 2004.

[64] X. Lansiaux *et al.*, "$LiNbO_3$ thick films grown on sapphire by using a multistep sputtering process," *J. Appl. Phys.*, vol. 90, no. 10, pp. 5274–5277, Nov. 2001.

[65] Y. Sakashita and H. J. Segawa, "Preparation and characterization of LiNbO3 thin films produced by chemicalvapor deposition," *J. Appl. Phys.*, vol. 77, no. 11, pp. 5995–5999, Jun. 1995.

[66] J. G. Yoon and K. Kim, "Growth of highly textured $LiNbO_3$ thin film on Si with MgO buffer layer through the sol-gel process," *Appl. Phys. Lett.*, vol. 68, no. 18, pp. 2523–2525, Apr. 1996.

[67] [Online]. Available: http://www.srim.org

[68] M. Levy *et al.*, "Fabrication of single-crystal lithium niobate films by crystal ion slicing," *Appl. Phys. Lett.*, vol. 73, no. 16, pp. 2293–2295, Oct. 1998.

[69] M. Bruel, "The history physics and applications of the smart-cut process," *MRS Bull*., vol. 23, no. 12, pp. 35–39, Dec. 1998.

[70] P. Rabiei and P. Günter, "Optical and electro-optical properties of submicrometer lithium niobate slab waveguides prepared by crystal ion slicing and wafer bonding," *Appl. Phys. Lett.*, vol. 85, no. 20, pp. 4603–4605, Nov. 2004.

[71] H. Hu, L. Gui, R. Ricken, and W. Sohler, "Towards nonlinear photonic wires in lithium niobate," *Proc. SPIE*, vol. 7604, 2010, Art. no. 76040R, doi:10.1117/12.842674.

[72] A. Rao and S. Fathpour, "Second-harmonic generation in integrated photonics on silicon," *Phys. Status Solidi A*, 2017, Art. no. 1700684.

[73] P. Rabiei, J. Ma, S. Khan, J. Chiles, and S. Fathpour, "Heterogeneous lithium niobate photonics on silicon substrates," *Opt. Express*, vol. 21, no. 21, pp. 25573–25581, Oct. 2013.

[74] D. Burdeaux, P. Townsend, J. Carr, and P. Garrou, "Benzocyclobutene (BCB) dielectrics for the fabrication of high-density, thin-film multichip modules," *J. Electron. Mater.*, vol. 19, no. 12, pp. 1357–1364, Dec. 1990.

[75] C. F. Kane and R. R. Krchnavek, "Benzocyclobutene optical waveguides," *IEEE Photon. Technol. Lett.*, vol. 7, no. 5, pp. 535–537, May 1995.

[76] A. Guarino, G. Poberaj, D. Rezzonico, R. Degl'Innocenti, and P. Gunter, "Electro–optically tunable microring resonators in lithium niobate," *Nat. Photon.*, vol. 1, pp. 407–410, Jul. 2007.

[77] G. Poberaj *et al.*, "Ion-sliced lithium niobate thin films for active photonic devices," *Opt. Mater.*, vol. 31, no. 7, pp. 1054–1058, May 2009.

[78] H. Takagi, R. Maeda, N. Hosoda, and T. Suga, "Room-temperature bonding of lithium niobate and silicon wafers by argon-beam surface activation," *Appl. Phys. Lett.*, vol. 74, no. 16, pp. 2387–2389, Apr. 1999.

[79] M. Howlader, T. Suga, and M. Kim, "Room temperature bonding of silicon and lithium niobate," *Appl. Phys. Lett.*, vol. 89, no. 3, Jul. 2006, Art. no. 031914.

[80] Y. S. Lee *et al.*, "Hybrid Si-$LiNbO_3$ microring electro-optically tunable resonators for active photonic devices," *Opt. Lett.*, vol. 36, no. 7, pp. 1119–1121, Apr. 2011.

[81] L. Chen, M. G. Wood, and R. M. Reano, "12.5 pm/V hybrid silicon and lithium niobate optical microring resonator with integrated electrodes," *Opt. Express*, vol. 21, no. 22, pp. 27003–27010, Nov. 2013.

[82] L. Chen, Q. Xu, M. G. Wood, and R. M. Reano, "Hybrid silicon and lithium niobate electro-optical ring modulator," *Optica*, vol. 1, no. 2, pp. 112–118, Aug. 2014.

[83] L. Chen, J. Chen, J. Nagy, and R. M. Reano, "Highly linear ring modulator from hybrid silicon and lithium niobate," *Opt. Express*, vol. 23, no. 10, pp. 13255–13264, May 2015.

[84] P. O. Weigel *et al.*, "Lightwave circuits in lithium niobate through hybrid waveguides with silicon photonics," *Sci. Rep.*, vol. 6, Mar. 2016, Art. no. 22301.

[85] J. Chiles and S. Fathpour, "Mid-infrared integrated waveguide modulators based on silicon-on-lithium-niobate photonics," *Optica*, vol. 1, no. 5, pp. 350–355, Nov. 2014.

[86] J. D. Witmer *et al.*, "High-Q photonic resonators and electro-optic coupling using silicon-on-lithium-niobate," *Sci. Rep.*, vol. 7, Apr. 2017, Art. no. 46313.

[87] L. Cao, A. Aboketaf, Z. Wang, and S. Preble, "Hybrid amorphous silicon (a-Si:H)–LiNbO3 electro-optic modulator," *Opt. Commun.*, vol. 330, pp. 40–44, Nov. 2014.

[88] A. J. Mercante *et al.*, "110 GHz CMOS compatible thin film $LiNbO_3$ modulator on silicon," *Opt. Express*, vol. 24, no. 14, pp. 15590–15595, Jul. 2016.

[89] G. R. Paz-Pujalt *et al.*, "Characterization of proton exchange lithium niobate waveguides," *J. Appl. Phys.*, vol. 76, no. 7, pp. 3981–3987, Oct. 1994.

[90] L. Cai, S. L. H. Han, and H. Hu, "Waveguides in single-crystal lithium niobate thin film by proton exchange," *Opt. Express*, vol. 23, no. 2, pp. 1240–1248, Jan. 2015.

[91] L. Cai, Y. Wang, and H. Hu, "Low-loss waveguides in a single-crystal lithium niobate thin film," *Opt. Lett.*, vol. 40, no. 13, pp. 3013–3016, Jul. 2015.

[92] L. Cai, R. Kong, Y. Wang, and H. Hu, "Channel waveguides and y-junctions in x-cut single-crystal lithium niobate thin film," *Opt. Express*, vol. 23, no. 22, pp. 29211–29221, Nov. 2015.

[93] P. Rabiei, J. Ma, J. Chiles, S. Khan, and S. Fathpour, "Submicron optical waveguides and microring resonators fabricated by selective oxidation of tantalum," *Opt. Express*, vol. 21, no. 6, pp. 6967–6972, Mar. 2013.

[94] P. Rabiei, A. Rao, J. Chiles, J. Ma, and S. Fathpour, "Low-loss and high index-contrast tantalum pentoxide microring resonators and grating couplers on silicon substrates," *Opt. Lett.*, vol. 39, no. 18, pp. 5379–5382, Sep. 2014.

[95] S. Li, L. Cai, Y. Wang, Y. Jiang, and H. Hu, "Waveguides consisting of single-crystal lithium niobate thin film and oxidized titanium stripe," *Opt. Express*, vol. 23, no. 19, pp. 24212–24219, Sep. 2015.

[96] A. Rao *et al.*, "Heterogeneous microring and mach-zehnder lithium niobate electro-optical modulators on silicon," in *Proc. Conf. Laser Electro-Opt.*, 2015, paper STu2F.4.

[97] A. Rao *et al.*, "Heterogeneous microring and Mach-Zehnder modulators based on lithium niobate and chalcogenide glasses on silicon," *Opt. Express*, vol. 23, no. 17, pp. 22746–22752, Aug. 2015.

[98] J. Chiles *et al.*, "Low-loss, submicron chalcogenide integrated photonics with chlorine plasma etching," *Appl. Phys. Lett.*, vol. 106, no. 11, Mar. 2015, Art. no. 111110.
[99] A. Rao *et al.*, "High-performance and linear thin-film lithium niobate Mach–Zehnder modulators on silicon up to 50 GHz," *Opt. Lett.*, vol. 41, no. 24, pp. 5700–5703, Dec. 2016.
[100] A. Rao *et al.*, "Second-harmonic generation in periodically-poled thin film lithium niobate wafer-bonded on silicon," *Opt. Express*, vol. 24, no. 26, pp. 29941–29947, Dec. 2016.
[101] A. Rao *et al.*, "Second-harmonic generation in single-mode integrated waveguides based on mode-shape modulation," *Appl. Phys. Lett.*, vol. 110, no. 11, Mar. 2017, Art. no. 111109.
[102] S. Jin, L. Xu, H. Zhang, and Y. Li, "$LiNbO_3$ thin-film modulators using silicon nitride surface ridge waveguides," *IEEE Photon. Technol. Lett.*, vol. 28, no. 7, pp. 736–739, Apr. 2016.
[103] H. Hu, R. Ricken, and W. Sohler, "Etching of lithium niobate: From ridge waveguides to photonic crystal structures," in *Proc. 14th Eur. Conf. Integr. Opt.*, 2008, pp. 75–78.
[104] H. Hu, R. Ricken, and W. Sohler, "Lithium niobate photonic wires," *Opt. Express*, vol. 17, no. 26, pp. 24261–24268, Dec. 2009.
[105] C. Wang *et al.*, "Integrated high quality factor lithium niobate microdisk resonators," *Opt. Express*, vol. 22, no. 25, pp. 30924–30933, Dec. 2014.
[106] I. Krasnokutska, J.-L. J. Tambasco, X. Li, and A. Peruzzo, "Ultra-low loss photonic circuits in lithium niobate on insulator," arXiv:1708.06787, 2017.
[107] R. R. Thomson, S. Campbell, I. J. Blewett, A. K. Kar, and D. T. Reid, "Optical waveguide fabrication in z-cut lithium niobate ($LiNbO_3$) using femtosecond pulses in the low repetition rate regime," *Appl. Phys. Lett.*, vol. 88, no. 11, Mar. 2006, Art. no. 111109.
[108] M. F. Volk, S. Suntsov, C. E. Rüter, and D. Kip, "Low loss ridge waveguides in lithium niobate thin films by optical grade diamond blade dicing," *Opt. Express*, vol. 24, no. 2, pp. 1386–1391, Jan. 2016.
[109] K. Higuma, S. Oikawa, Y. Hashimoto, H. Nagata, and M. Izutsu, "X-cut lithium niobate optical single-sideband modulator," *Electron. Lett.*, vol. 37, no. 8, pp. 515–516, Apr. 2001.
[110] L. Cai, Y. Kang, and H. Hu, "Electric-optical property of the proton exchanged phase modulator in single-crystal lithium niobate thin film," *Opt. Express*, vol. 24, no. 5, pp. 4640–4647, Mar. 2016.
[111] C. Wang, M. Zhang, B. Stern, M. Lipson, and M. Loncar, "Nanophotonic lithium niobate electro-optic modulators," arXiv:1701.06470, 2017.
[112] C. Cox, E. Ackerman, G. Betts, and J. Prince, "Limits on the performance of RF-over-fiber links and their impact on device design," *IEEE Trans. Microw. Theory Techn.*, vol. 54, no. 2, pp. 906–920, Feb. 2006.
[113] J. Capmany and D. Novak, "Microwave photonics combines two worlds," *Nat. Photon.*, vol. 1, pp. 319–330, Jun. 2007.
[114] J. P. Yao, "Microwave photonics," *J. Lightw. Technol.*, vol. 27, no. 3, pp. 314–335, Feb. 2009.
[115] W. D. Sacher and J. K. S. Poon, "Dynamics of microring resonator modulators," *Opt. Express*, vol. 16, no. 20, pp. 15741–15753, Sep. 2008.
[116] K. Kubota, J. Noda, and O. Mikami, "Traveling wave optical modulator using a directional coupler $LiNbO_3$ waveguide," *IEEE J. Quantum Electron.*, vol. QE-16, no., pp. 754–760, Jul. 1980.
[117] C. J. Huang *et al.*, "Development of photonic devices for MMW sensing and imaging," *Proc. SPIE*, vol. 6232, 2006, Art. no. 62320Q.
[118] J. A. Ibarra Fuste and M. C. Santos Blanco, "Bandwidth-length trade-off figures of merit for electro-optic traveling wave modulators," *Opt. Lett.*, vol. 38, no. 9, pp. 1548–1550, May 2013.
[119] R. DeSalvo *et al.*, "The convergence of microwave photonic and optical wireless systems with military communication and sensor systems," in *Proc. Avionics Veh. Fiber-Opt. Photon. Conf.*, Long Beach, CA, USA, 2016, pp. 191–192, Art. no. WA2.1.
[120] C. Schuetz, "Optical techniques for millimeter-wave detection and imaging," Ph.D. dissertation, Dept. Elect. Comput. Eng., Univ. Delaware, Newark, DE, USA, 2007.
[121] L. Chen and R. M. Reano, "Compact electric field sensors based on indirect bonding of lithium niobate to silicon microrings," *Opt. Express*, vol. 20, no. 4, pp. 4032–4038, Feb. 2012.
[122] K. Mehta, G. West, and R. Ram, "SiN-on-$LiNbO_3$ integrated optical modulation at visible wavelengths," in *Proc. Conf. Lasers Electro-Optics*, 2017, Paper STu3N.7.

Ashutosh Rao (S'16) received the B.Tech. and M.Tech. degrees in engineering physics from the Indian Institute of Technology Bombay, Mumbai, India, in 2013. He is currently working toward the Ph.D. degree at the Center for Research and Education in Optics and Lasers, The College of Optics and Photonics, University of Central Florida, Orlando, FL, USA.

His research has included demonstrations of high-speed electrooptic modulators, second-order nonlinear optical frequency converters, and photon-pair generation in thin-film lithium niobate waveguides. His current research interests include integrated photonics, electrooptics, nonlinear optics, and quantum optics. He is a coauthor of more than 30 journal and conference papers.

Sasan Fathpour (S'01–M'04–SM'13) is an Associate Professor at the Center for Research and Education in Optics and Lasers, The College of Optics and Photonics, University of Central Florida, Orlando, FL, USA, and the Ph.D. degree in electrical engineering from the University of Michigan, Ann Arbor, MI, USA, in 2005. He then joined the Electrical Engineering Department, University of California Los Angeles, Los Angeles, CA, USA, as a Postdoctoral Fellow and joined the CREOL faculty in 2008. He is the coeditor of a book entitled *Silicon Photonics for Telecommunications and Biomedicine* (CRC Press, 2012), and a coauthor of more than 150 journal and conference papers, book chapters, and patents. His current research interests include heterogeneous integrated photonics, nonlinear integrated optics, silicon photonics, and nonconventional optical waveguide platforms for mid-wave infrared and other applications.

Dr. Fathpour is a recipient of UCF Reach for the Stars Award (2015), the ONR Young Investigator Award (2013), the NSF CAREER Award (2012), and the UCLA Chancellor's Award for Postdoctoral Research (2007). He is a Fellow of OSA, the Optical Society, and a Senior Member of SPIE.